

failure over large areas. This implies that the critical feature at play in the generation of mega-earthquakes is not the amplitude of shear strength but its spatial variations. Thus, the absence of asperities on large faults may counterintuitively be a source of higher hazard. Though our study focused on subduction earthquakes, flatness may favor large earthquakes on long strike-slip faults as well.

REFERENCES AND NOTES

- H. Kanamori, *Philos. Trans. R. Soc. A* **364**, 1927–1945 (2006).
- L. Ruff, H. Kanamori, *Phys. Earth Planet. Inter.* **23**, 240–252 (1980).
- L. Ruff, H. Kanamori, *Tectonophysics* **99**, 99–117 (1983).
- R. McCaffrey, *Geophys. Res. Lett.* **21**, 2327–2330 (1994).
- S. Stein, E. A. Okal, *Bull. Seismol. Soc. Am.* **97**, S279–S295 (2007).
- T. Nishikawa, S. Ide, *Nat. Geosci.* **7**, 904–908 (2014).
- Q. Bletery et al., *J. Geophys. Res. Solid Earth* **119**, 7636–7653 (2014).
- R. D. Müller, M. Sdrolias, C. Gaina, W. R. Roest, *Geochem. Geophys. Geosyst.* **9**, Q04006 (2008).
- T.-R. A. Song, M. Simons, *Science* **301**, 630–633 (2003).
- R. E. Wells, R. J. Blakely, Y. Sugiyama, D. W. Scholl, P. A. Dinterman, *J. Geophys. Res. Solid Earth* **108**, 2507 (2003).
- W. Schellart, N. Rawlinson, *Phys. Earth Planet. Inter.* **225**, 41–67 (2013).
- A. Heuret, C. Conrad, F. Funicello, S. Lallemand, L. Sandri, *Geophys. Res. Lett.* **39**, L05304 (2012).
- J. F. Pacheco, L. R. Sykes, *Bull. Seismol. Soc. Am.* **82**, 1306 (1992).
- G. P. Hayes, D. J. Wald, R. L. Johnson, *J. Geophys. Res. Solid Earth* **117**, B01302 (2012).
- X. Gao, K. Wang, *Science* **345**, 1038–1041 (2014).
- C. H. Scholz, J. Campos, *J. Geophys. Res. Solid Earth* **117**, B05310 (2012).
- R. Madariaga, *J. Geophys. Res.* **84**, 2243 (1979).
- H. Kanamori, D. L. Anderson, *J. Geophys. Res.* **80**, 1075–1078 (1975).
- Materials and methods are available as supplementary materials on Science Online.
- P. A. McCrory, J. L. Blair, F. Waldhauser, D. H. Oppenheimer, *J. Geophys. Res. Solid Earth* **117**, n/a (2012).
- W. P. Schellart, J. Freeman, D. R. Stegman, L. Moresi, D. May, *Nature* **446**, 308–311 (2007).
- A. F. Holt, B. A. Buffett, T. W. Becker, *Geophys. Res. Lett.* **42**, 3802–3810 (2015).
- W. Schellart, *J. Geophys. Res. Solid Earth* **115**, B11406 (2010).
- T. Lay, H. Kanamori, L. Ruff, *Earthq. Predict. Res.* **1**, 3 (1982).
- S. T. Tse, J. R. Rice, *J. Geophys. Res.* **91**, 9452 (1986).
- Q. Dieterich, *J. Geophys. Res. Solid Earth* **99**, 2601–2618 (1994).
- C. H. Scholz, *Nature* **391**, 37–42 (1998).
- C. Marone, *Nature* **391**, 69–72 (1998).
- Y. Guglielmi, F. Cappa, J.-P. Avouac, P. Henry, D. Elsworth, *Science* **348**, 1224–1226 (2015).
- B. P. Allmann, P. M. Shearer, *J. Geophys. Res. Solid Earth* **114**, B01310 (2009).
- K. Wang, S. L. Bilek, *Tectonophysics* **610**, 1–24 (2014).
- K. Wang, S. L. Bilek, *Geology* **39**, 819–822 (2011).
- Q. Bletery, A. Sladen, J. Jiang, M. Simons, *J. Geophys. Res. Solid Earth* **121**, 5116–5135 (2016).
- R. McCaffrey, *Geology* **36**, 263 (2008).
- K. Satake, K. Wang, B. F. Atwater, *J. Geophys. Res. Solid Earth* **108**, 2535 (2003).
- T. Furumura, K. Imai, T. Maeda, *J. Geophys. Res. Solid Earth* **116**, B02308 (2011).
- F. Dahlen, *Annu. Rev. Earth Planet. Sci.* **18**, 55–99 (1990).
- R. J. Lisle, J. M. Robinson, *J. Struct. Geol.* **17**, 739–750 (1995).
- C. R. Ranero, J. Phipps Morgan, K. McIntosh, C. Reichert, *Nature* **425**, 367–373 (2003).
- M. Faccenda, T. V. Gerya, L. Burlini, *Nat. Geosci.* **2**, 790–793 (2009).
- T. Nishikawa, S. Ide, *Geophys. Res. Lett.* **42**, 7081–7089 (2015).

ACKNOWLEDGMENTS

We thank R. Bürgmann for his valuable comments on the manuscript. The slab1.0 model is available online at <http://earthquake.usgs.gov/data/slab/>. The U.S. Geological Survey catalog of historical earthquakes ($M \geq 8.0$ since 1900) that we used in this

study can be found at <http://earthquake.usgs.gov/earthquakes/world/historical.php>. For the subduction zones that have not experienced any $M \geq 8.0$ earthquakes since 1900, this catalog was complemented by the Global Centroid Moment Tensor catalog (www.globalcmt.org/). We used Generic Mapping Tools to compute the distributions of dip-angle gradients (gmt.soest.hawaii.edu/). This work was supported by NSF grant EAR-1520238, ANR project TO-EOS, and the French Ministry of Research and Education.

SUPPLEMENTARY MATERIALS

www.sciencemag.org/content/354/6315/1027/suppl/DC1
Materials and Methods
Figs. S1 to S8
Tables S1 to S2
References (42–53)

6 May 2016; accepted 19 October 2016
10.1126/science.aag0482

CATALYSIS

Direct and continuous strain control of catalysts with tunable battery electrode materials

Haotian Wang,¹ Shicheng Xu,² Charlie Tsai,^{3,4} Yuzhang Li,⁵ Chong Liu,⁵ Jie Zhao,⁵ Yayuan Liu,⁵ Hongyuan Yuan,⁶ Frank Abild-Pedersen,⁴ Fritz B. Prinz,^{2,5} Jens K. Nørskov,^{3,4} Yi Cui^{5,7*}

We report a method for using battery electrode materials to directly and continuously control the lattice strain of platinum (Pt) catalyst and thus tune its catalytic activity for the oxygen reduction reaction (ORR). Whereas the common approach of using metal overlayers introduces ligand effects in addition to strain, by electrochemically switching between the charging and discharging status of battery electrodes the change in volume can be precisely controlled to induce either compressive or tensile strain on supported catalysts. Lattice compression and tension induced by the lithium cobalt oxide substrate of ~5% were directly observed in individual Pt nanoparticles with aberration-corrected transmission electron microscopy. We observed 90% enhancement or 40% suppression in Pt ORR activity under compression or tension, respectively, which is consistent with theoretical predictions.

Highly efficient electrocatalysts for renewable energy conversion processes, such as in H₂ fuel cells and water-splitting electrocatalysis, is becoming increasingly important (1–3). One strategy for systematically improving the activities of known catalysts is to modify their electronic structure (4–6). Numerous examples have been demonstrated in H₂O–O₂–H₂ electrocatalysis, such as the changing of d band filling in perovskite oxides for oxygen evolution (7), transition-metal alloying for the oxygen reduction reaction (ORR) (4, 8–11), and our recent studies of using lithium (Li)-ion intercalation and extraction in layered materials for water-splitting (12, 13).

Lattice strain, either compressive or tensile, can alter the surface electronic structure by mod-

ifying the distances between surface atoms and in turn catalytic activity (14–17). For platinum (Pt), previous studies have suggested that the 5d-band center of Pt can be shifted by ~0.1 eV with only 1% lattice strain (18), which can appreciably strengthen or weaken bonding of reaction intermediates to the surface (14, 18). Lattice-mismatch between metals can be generated by directly synthesizing core-shell structures (19–23) or by selectively removing atoms from an alloy (for example, stripping away Cu from a Pt-Cu alloy) (8, 14, 24–26). However, because of the larger lattice of Pt as compared with that of most metal cores, this method is typically restricted to compressive strain (14, 27). Additionally, both electronic charge transfer between the different metal atoms (ligand effects) and changes in the surface stability—and thus surface area—are present, making it difficult to identify and control the effects of strain alone (14, 25). Another strategy is to deposit catalysts onto flat substrates that undergo physical transformations as external forces are applied or the temperatures varied (28, 29). Those flat and tunable substrates present great importance to fundamental analysis, but only a few of them have been successfully demonstrated effective in electrocatalysis (28). Thus, new methods that can flexibly and effectively control both tensile and compressive lattice strain in catalysts without introducing additional effects are needed.

¹Department of Applied Physics, Stanford University, Stanford, CA 93205, USA. ²Department of Mechanical Engineering, Stanford University, Stanford, CA 93205, USA. ³SUNCAT Center for Interface Science and Catalysis, Department of Chemical Engineering, Stanford University, Stanford, CA 94305, USA. ⁴SUNCAT Center for Interface Science and Catalysis, SLAC National Accelerator Laboratory, 2575 Sand Hill Road, Menlo Park, CA 94025, USA. ⁵Department of Material Science and Engineering, Stanford University, Stanford, CA 94305, USA. ⁶Department of Physics, Stanford University, Stanford, CA 94305, USA. ⁷Stanford Institute for Materials and Energy Sciences, SLAC National Accelerator Laboratory, 2575 Sand Hill Road, Menlo Park, CA 94025, USA.

*Corresponding author. Email: ycui@stanford.edu

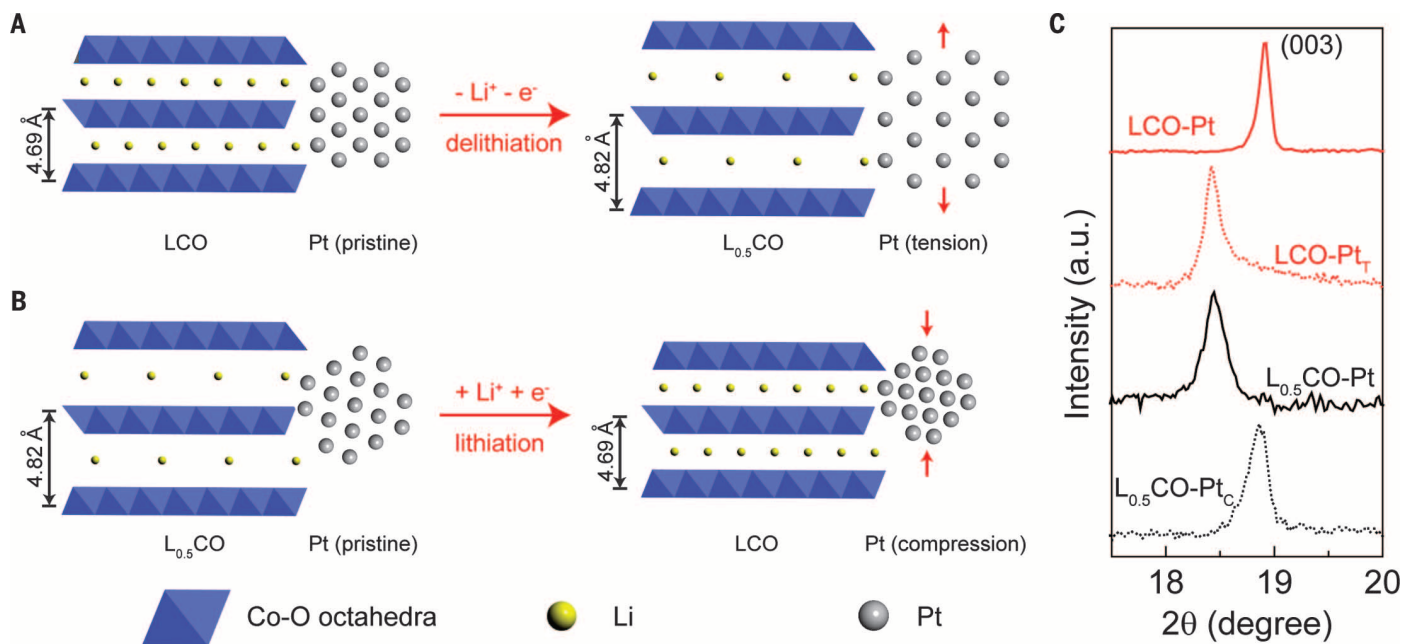


Fig. 1. Schematic of the lattice constant change of LCO substrates and how the lattice strains are induced to Pt NPs. (A) Pristine LCO shows a Co-O layer spacing of 4.69 Å. By electrochemically extracting half of the Li ions out, the layer spacing is increased to 4.82 Å. (B) LCO is first delithiated into $L_{0.5}CO$ with layers expanded and then coated with Pt NPs. By intercalating back those Li ions, the Co-O layer spacing is decreased so as to induce compression on Pt NPs. The orientation of Pt NP is set to be different from (A) as a suggestion of nonepitaxial ALD growth. (C) The XRD peak shifts of LCO (003) represent the tensile and compressive strain induced to Pt NPs coated on these substrates.

We report a way to tune catalyst strain by exploiting the widely tunable lattice constant of Li-ion battery electrode materials as the catalyst support. When Li ions are electrochemically intercalated into or extracted out of electrode materials such as graphite, transition-metal dichalcogenides, silicon (Si), or Li metal oxides, the volume and lattice spacing change from several percent to severalfold (12, 30–32). For example, the Si electrode can expand up to four times its original size when fully lithiated to $Li_{4.4}Si$ (30), and $LiCoO_2$ (LCO) undergoes ~3% volume changes during charge and discharge (31, 33). This smaller value is still sufficient to generate strain that can alter catalysis. Li ions are sandwiched by Co-O octahedra slabs in LCO (Fig. 1A) (34), and during charging, half of the Li^+ are extracted to form $Li_{0.5}CoO_2$ ($L_{0.5}CO$). The Co-O slabs with negative charge experience stronger electrostatic repulsions from each other, which increases the layer spacing (Fig. 1A) (31, 33). When Li^+ intercalates back during discharge, the lattice returns to its original spacing (Fig. 1B).

We deposited small Pt nanoparticles (NPs; ~5 nm) onto the surface of LCO or $L_{0.5}CO$ particle supports (~500 nm). By controlling the charging or discharging states of the substrate, we directly observed ~5% compressive and tensile strain on Pt (111) facets using transmission electron aberration-corrected microscopy (TEAM) in individual particles. The ORR catalytic activities of Pt NPs in alkaline solution were tuned over a wide range, achieving nearly 90% improvement or more than 40% decrease in activity under compressive and tensile strain, respectively. These

results agree well with predictions from density functional theory (DFT) calculations.

Our strategy for introducing and controlling strain is shown in the schematic in Fig. 1. We obtained the battery electrode material LCO using a cotton-assisted pyrolysis method (35). The sizes of LCO particles are ~500 nm in the scanning electron microscopy (SEM) images (fig. S1, A and B) (35). We then used 150 cycles of atomic layer deposition (ALD) to deposit ~5 nm Pt NPs onto the surface of LCO (LCO-Pt) (figs. S2A and S3). The reason for this small loading is that (i) strain decays from substrate to the top surface and (ii) the gaps between Pt NPs are important for Li-ion transport into and out of LCO.

To induce lattice tension on the Pt NPs, LCO-Pt was assembled in a battery cell for the electrochemical charging process, with half of the Li ions extracted (LCO-Pt_T) (fig. S4). The x-ray diffraction (XRD) peak corresponding to the LCO (003) facets shifted from 18.92° to 18.42° in Fig. 1C, corresponding to an increase in layer spacing from 4.69 to 4.82 Å (Fig. 1A) (35). This nearly 3% expansion in the substrate can induce strong uniaxial tension on Pt NPs (28). Expansion in other LCO facets was also observed during the delithiation process (fig. S5).

Compressive strain on Pt catalyst was achieved with a reverse process (Fig. 1B). LCO substrate was first electrochemically delithiated to be $L_{0.5}CO$ with layers opened up, and then followed by ALD growth of Pt NPs ($L_{0.5}CO$ -Pt). No appreciable differences in the morphology were observed when transforming from LCO and LCO-Pt to $L_{0.5}CO$ and $L_{0.5}CO$ -Pt, respectively (figs. S1, C and D, and

S2B). By intercalating Li ions into $Li_{0.5}CO$ -Pt, the distances in the molecular layer decreased back to that of LCO, creating compressive strain on Pt NPs ($L_{0.5}CO$ -Pt_C). This change was also confirmed by the XRD peaks in Fig. 1C. Because of the shift in the lattice between LCO/ $L_{0.5}CO$ in the z direction (4.69 versus 4.82 Å) and Pt (3.92 Å), we suspect that the ALD growth of Pt NPs on LCO and $L_{0.5}CO$ substrates was not epitaxial and thus did not introduce strain (36–39). TEAM characterization revealed different Pt orientations relative to the supports (fig. S6). With strong bonding between Pt and LCO/ $L_{0.5}CO$, the expansion or compression of substrates would lead to lattice strains in the catalysts.

Because of the broadening of peaks for small Pt NPs as well as the wide distribution of strain in different Pt NPs, XRD is insufficient for accurately determining the amount of strain on different sites of substrates (fig. S7). Instead, we used high-resolution TEAM, as shown in Fig. 2 (35). For compressive strain, a comparison between the pristine $L_{0.5}CO$ -Pt and the compressed $L_{0.5}CO$ -Pt_C is shown in Fig. 2, A to D, and similarly for tensile strain for LCO-Pt_T in Fig. 2, E to H. We focus on Pt (111) as a representative facet for studying the lattice strain as well as catalytic activities. For a fair comparison, Pt NPs with the [110] direction in the zone axis were selected in all of the four samples, thus providing the lattice spacing for the (111), (11 $\bar{1}$), and (002) facets in the TEAM images. In addition, the Co-O layers of LCO are parallel to the TEAM electron beam (fig. S8), which suggests the uniaxial strain direction applied on those Pt NPs. As indicated in Fig. 2,

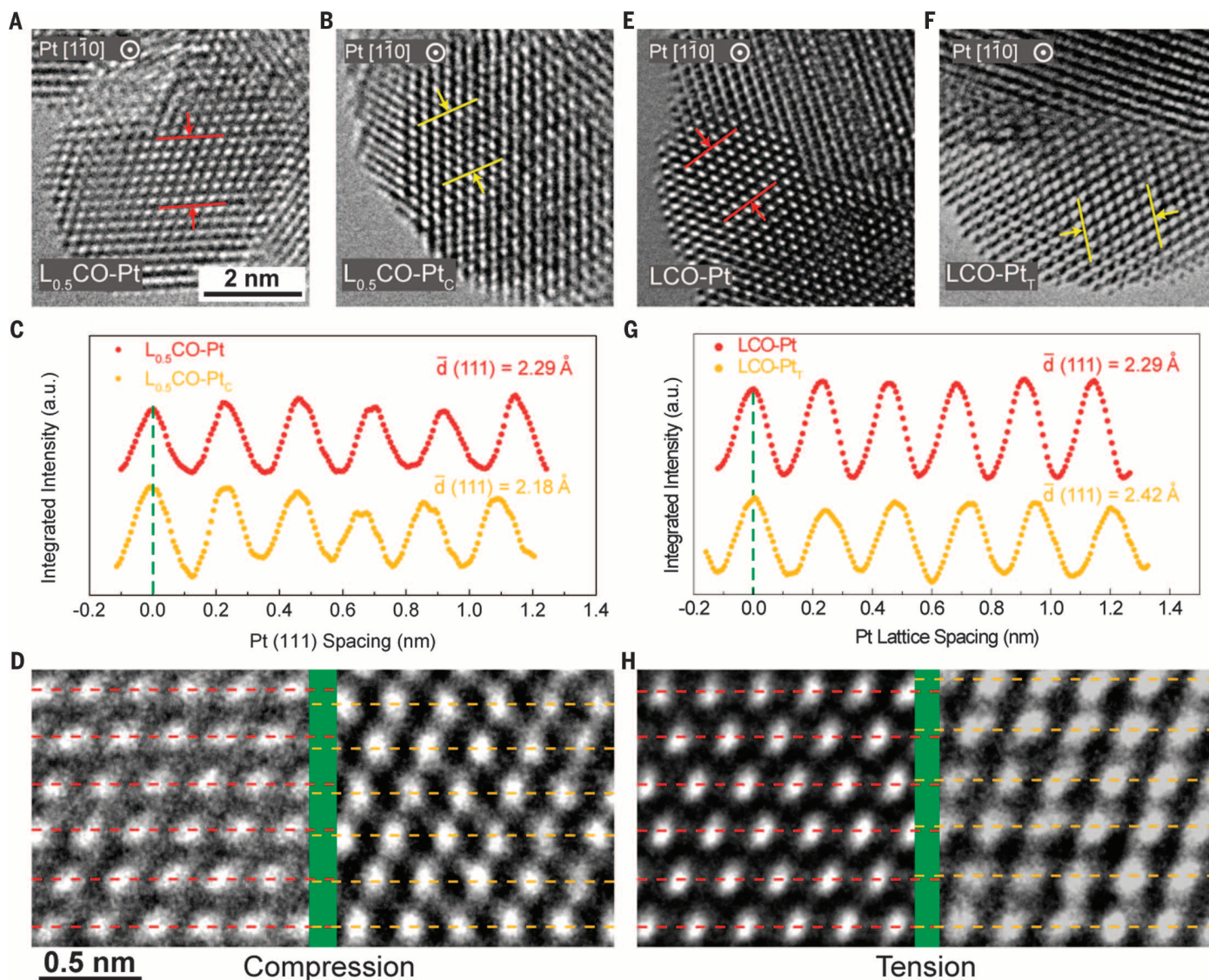


Fig. 2. High-resolution TEAM images of pristine and strained Pt NPs with (111) lattice compression and tension. Compression, (A) to (D); tension, (E) to (H). (A and B) TEAM images of $L_{0.5}\text{CO-Pt}$ and $L_{0.5}\text{CO-Pt}_C$. The red and yellow bars denote the areas we analyzed for (111) spacing. (C) The integrated pixel intensities of pristine and compressed Pt along (111) spacing directions (which is perpendicular to the facets). The peaks and valleys represent the atoms and gaps, respectively. The spacing of Pt (111) facets is averaged over six atomic layers for high accuracy. The pristine (111) is measured to be 2.29 Å, whereas the constrained (111) shows only 2.18 Å. (D) The bottom layers of pristine and compressed Pt (111) lattice fringes are aligned for the direct evidence of lattice constraint. The top atomic layer of compressed Pt locates at a much lower position than the pristine one. (E and F) TEAM images of LCO-Pt and LCO-Pt_T. (G) More than 5% tensile strain is observed with an increased (111) spacing of 2.42 Å. (H) A direct evidence of tensile strain with the top atomic layer of LCO-Pt_T much higher than that of LCO-Pt. Another example of tensile strain is also shown and aligned in figs. S13 and S14. (A), (B), (E), and (F) share the same scale bar, and (D) and (H) share the same scale bar.

A, B, E, and F, we examined the central regions of the Pt NPs and obtained the averaged (111) facet spacing over six atomic layers, avoiding possible surface defects as well as blurry boundaries between Pt and the substrates.

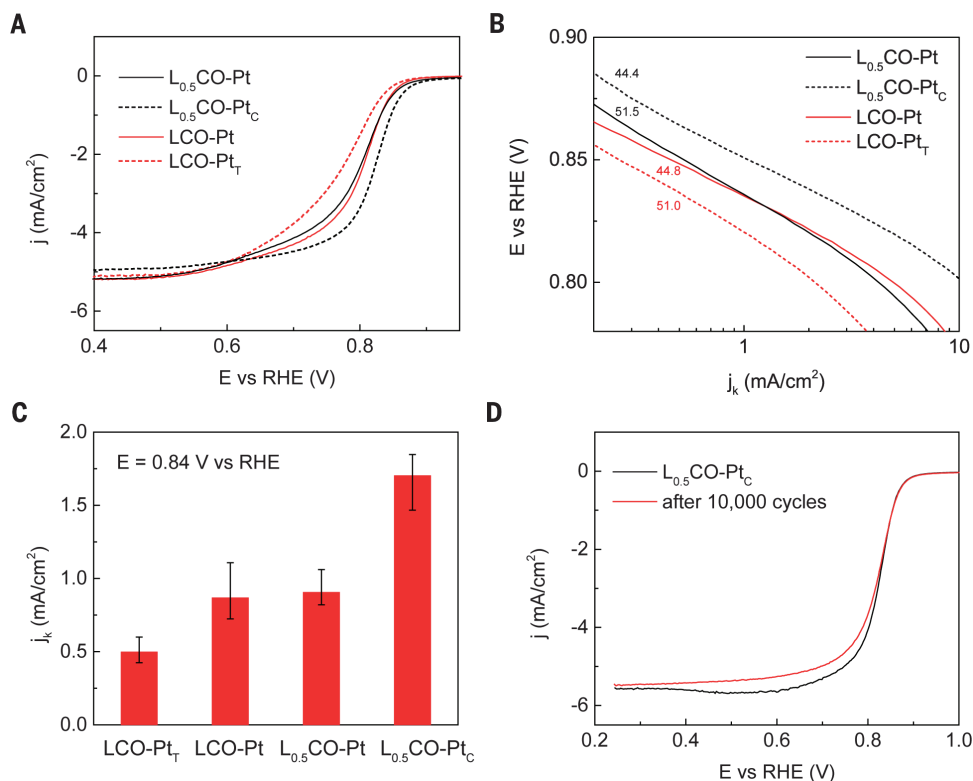
Shown in Fig. 2C are the integrated pixel intensities for the pristine and compressed Pt (111) lattices as selected in Fig. 2, A and B, respectively (35). The averaged pristine Pt (111) spacing is 2.29 Å, which agrees well with calculations from previously reported Pt lattice constants (35). The intensity profile of constrained Pt suggests a much smaller lattice distance compared with that of the pristine Pt, with an averaged spacing of 2.18 Å,

which represents ~5% compressive strain. This 5% lattice strain appears to be even greater than the lattice change of the LCO substrate (~3%), which can be explained by a possible inhomogeneity of the Li concentration near the LCO surface and within the bulk during the charging or discharging processes (40). The surfaces may have a greater change in Li concentration and thus lead to larger changes in the lattice. For example, the $L_{0.25}\text{CO}$ lattice can expand ~6.3% from LCO, which doubles the expansion of $L_{0.5}\text{CO}$ (41).

To have an intuitive understanding of how much the compressive lattice strain is, we aligned the (111) atomic layers on the bottom in Fig. 2D.

After five layers of accumulation in spacing differences, the top layer of compressed Pt locates to a much lower position than that of the pristine Pt, offering direct evidence of the lattice compression. The successful observation of compressive strain in the Pt (111) facet led us to study whether there were any changes in the other two facets, (11 $\bar{1}$) and (002), as well as the angles between them (figs. S9 and S10) (42). However, the spacing of these two facets in the compressed Pt NP is consistent with that of the unstrained catalyst, and we observed only slight distortions in the plane angles. This difference is caused by the direction of uniaxial strain applied by the LCO

Fig. 3. Electrochemical characterizations of pristine and strained Pt NPs in O₂-saturated 0.1 M KOH for ORR electrocatalysis. (A) The ORR polarization curves L_{0.5}CO-Pt, L_{0.5}CO-Pt_C, LCO-Pt, and LCO-Pt_T under 1600 rotations per minute (rpm). The pristine Pt NPs on LCO and L_{0.5}CO substrates show negligible differences in ORR activity. Compressive strain shows an improved ORR activity, and tensile strain shows a decreased one. (B) The Tafel slopes of pristine and strained Pt NPs. j_k represents the kinetic current density. (C) The comparison of ORR activities under 0.84 V versus RHE. The error bars are based on at least three identical samples for each condition. (D) The ORR polarizations of compressive L_{0.5}CO-Pt_C before and after 10,000 CV cycles between 0.6 and 1.0 V versus RHE.



substrate being perpendicular to Pt (111) facets (fig. S8), resulting in outstanding lattice constraint in the (111) but not the (11 $\bar{1}$) or (002) facets. However, because there are different Pt orientations on LCO/L_{0.5}CO substrates (fig. S6), the strain applied by the substrates is not always perpendicular to Pt (111) but also to other facets, which can induce strains in other facets.

Tensile strain was also revealed with TEAM (Fig. 2, E to H) by directly aligning the expanded Pt (111) planes with the pristine one in Fig. 2H, with the averaged spacing increased from 2.29 Å toward 2.42 Å (figs. S11 and S12). This roughly 5.7% expansion, together with the demonstrated compression, strongly suggests the efficacy of a LCO battery electrode in flexibly tuning lattice strain in both tensile and compressive directions over a full range of ~10%. The observed Pt (111) lattice strains in individual NPs can only represent a general trend (compression or tension) of the NP systems, as suggested in the Pt XRD peak shifts (fig. S7). We have included additional TEAM examples of Pt lattice strain (figs. S13 to S16) with different strain ranges. These Pt NPs have similar sizes with those in Fig. 2 but show different strain ranges, demonstrating that the particle size is not the only factor in determining the lattice strain. The strain condition in each Pt NP is strongly affected by its shape, crystallinity, location, and surface defects, as well as the contact facets of both the Pt particle and the LCO substrate. In addition, we also performed aberration-corrected scanning transmission electron microscope high-angle annular dark-field (STEM-HAADF) imaging on the tensile strain case in order to suppress the substrate effects on Pt NPs in TEM characterizations

(figs. S17 to S19). Convergent beam electron diffraction (CBED) of pristine and tensile Pt NPs is also shown in figs. S20 to S22, further demonstrating the existence of lattice strain introduced by the support.

The relation between Pt lattice strain and its ORR catalytic activities was examined in a rotating-disc three-electrode system (35). Four samples were tested: L_{0.5}CO-Pt and L_{0.5}CO-Pt_C for studying compressive strain and LCO-Pt and LCO-Pt_T for tensile strain. The mass ratio of Pt in those catalysts was determined to be ~17% (table S1) (35). Several cycles of cyclic voltammetry (CV) were applied before testing their ORR activities (fig. S23). In the polarization curves in Fig. 3A, the compressed Pt compared with the pristine catalyst presents a positive shift in onset as well as half-wave potentials by ~20 mV. In contrast, tensile strain induced a negative effect on ORR activity, requiring a larger overpotential to drive the reaction. The catalytic activity shifts caused by strain are consistent with previous works (14, 25, 27, 28). Background contributions from L_{0.5}CO and LCO substrates have been ruled out (fig. S24) (28). Because of the high density of free electrons in Pt metal, the charge transfer effects from the semiconducting support can be easily screened within one or two Pt atomic layers and will not affect the electronic properties of Pt surface sites for catalysis. We plotted the kinetic current densities of the pristine and strained samples versus potential and obtained their Tafel slopes in Fig. 3B, suggesting similar Tafel slopes ranging from 44.4 to 51.5 mV/decade within the measurement errors (fig. S25). The kinetic activities of pristine and strained Pt under 0.84 V potential are compared in Fig. 3C. The pristine Pt

on both L_{0.5}CO and LCO substrates shows similar activities at around 0.9 mA/cm², which is elevated to 1.7 mA/cm² under the compressive strain, representing a nearly doubled enhancement, but expanding the lattice of Pt NPs caused the ORR activity to decrease to only 0.5 mA/cm². The pristine L_{0.5}CO-Pt sample shows nearly the same ORR activity after 10,000 CV cycles (fig. S24), suggesting the good stability of Pt NPs on the LCO/L_{0.5}CO support as well as the strong interaction between them. In addition, the effect of lattice strain can also sustain during this long-term stability test without noticeable degradation, except for a slightly smaller diffusion-limiting current (Fig. 3D), which indicates that the strain effect does not affect its ORR stability.

Comparisons can be made of the data in Fig. 3 with our present theoretical model of the ORR (35). The close-packed Pt surfaces are most active for ORR (43), so we focused on the Pt (111) facets. The effect of strain on the adsorption free energies ΔG_i of the reaction intermediates ($i = \text{O}^*$, OH^* , and OOH^*), which are strongly related with the Pt 5d band (fig. S26), is illustrated in Fig. 4A. These adsorption energies are computed as $\Delta G_i = \Delta E_i + \Delta \text{ZPE} - \text{TAS}$, where ΔE_i is the formation of an intermediate i relative to H₂O and H₂, accounting for solvent-induced stabilizations; ΔZPE is the difference in zero point energies; and ΔS is the change in entropy (43). All quantities in Fig. 4A were determined relative to the unstrained Pt (111), which is defined as zero. Negative ΔG represents stronger binding, and positive ones represent weaker binding. For uniaxial strain in the range of 5% (tensile) to -5% (compressive), the adsorption free energies for all reaction

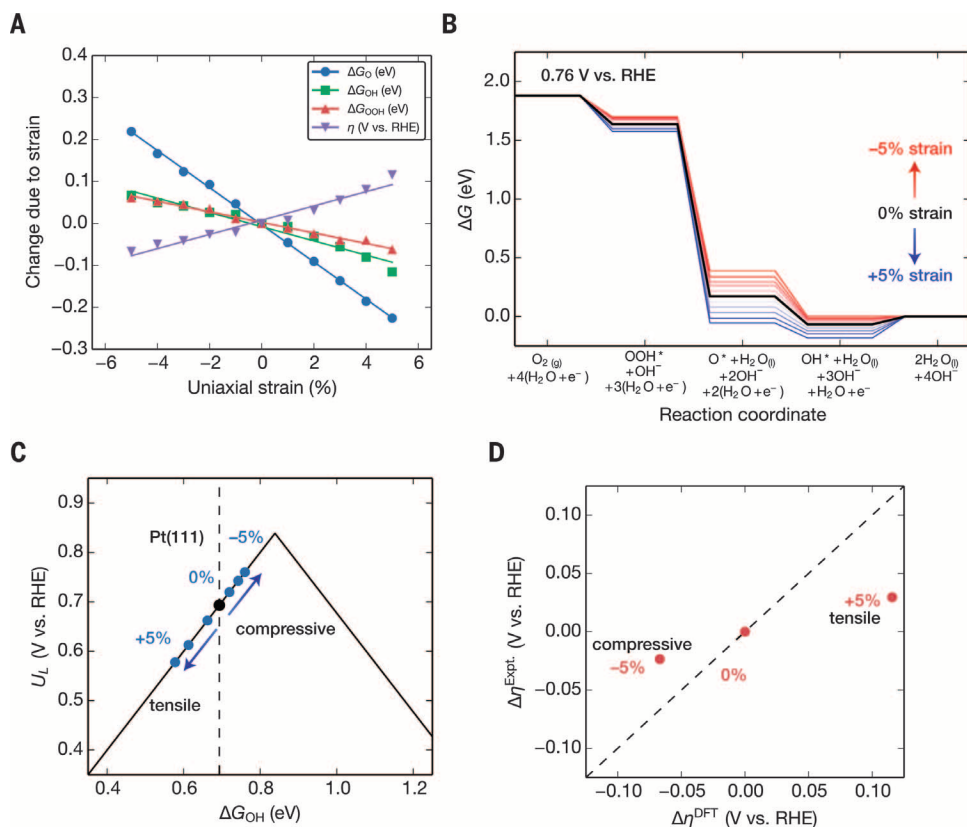


Fig. 4. Theoretical predictions for the effect of uniaxial strain on the Pt ORR activity. (A) The change in binding energies for O*, OH*, and OOH* intermediates as well as the change in the overpotential η as a function of uniaxial strain. The lines are linear fits to the data points. (B) The free-energy diagram for ORR at 0.76 V versus RHE, where all steps for the -5% strained Pt (111) are exergonic. The change in stabilities for each step caused by uniaxial strain is shown in red (compressive) and blue (tensile). (C) Illustration of the limiting potential “volcano” as a function of the change in ΔG_{OH} . The U_L improved with increasing compressive strain. The intermediate strains are ± 2 and $\pm 4\%$. (D) Comparisons between the change in experimental half-wave potential and the change in theoretical overpotential caused by strain. $\pm 5\%$ strain was chosen for the DFT values, corresponding to our TEM results in Fig. 2.

intermediates decrease (stronger binding) with tensile strain and increase (weaker binding) with compressive strain (17). Changes in ΔG_{OH} and ΔG_{OOH} are the same, whereas ΔG_{O} has a stronger dependence caused by its threefold coordination to the surface (44). The strain effects on these reaction intermediates have all been included in the free energy diagram in Fig. 4B, in which the free energy for each step was determined by adding a potential-dependence for ΔG_i using the computational hydrogen electrode model (45).

Because tensile strain makes the binding of all intermediates stronger, and $\text{OH}^* + \text{H}^+ + e^- \rightarrow \text{H}_2\text{O}(\text{l})$ is the limiting step for pristine Pt (43, 45), the thermodynamic sink for this final step only becomes deeper with tensile strain. Compressive strain weakens OH^* binding and leads to more facile desorption of the final product, $\text{H}_2\text{O}(\text{l})$. The theoretical overpotential η [defined as the potential over the equilibrium potential of 1.23 V versus reversible hydrogen electrode (RHE) required to make all reaction steps exergonic] thus decreases with compressive strain (becomes more active) and increases with expansive strain (becomes less active). At the applied potential of 0.76 V versus RHE, all steps become exergonic for the maximum -5% strain. The applied potential required to make all steps in the pathway exergonic is known as the limiting potential U_L . A lower U_L thus indicates higher activity. The binding energies of all intermediates scale linearly with one another (45, 46), which means that the energy for a single intermediate is sufficient for describing the entire pathway. Thus, U_L can be determined solely on the basis of the binding

strength of one of the intermediates, such as ΔG_{OH} . The ORR activity based on U_L as a function of ΔG_{OH} (a descriptor for all reaction intermediates) is illustrated by the volcano relation in Fig. 4C, in which the theoretical maximum limiting potential U_L occurs at ΔG_{OH} 0.84 eV. On the left leg, the limiting step is final H_2O desorption with $U_L = \Delta G_{\text{OH}}$, whereas on the right leg, the limiting step is the initial OOH^* adsorption. The peak arises from the aforementioned linear scaling between the binding strengths of OH^* and OOH^* (45, 46), which prevents them from being modified independently. For the same reason, we could also use ΔG_{O} or ΔG_{OOH} as the descriptor for Fig. 4C, with no changes in trends of the volcano plot. Regardless, compressive strain of $\sim 5\%$ should lead to improved activity toward the ORR. Although the 5% strain is not representative of all Pt particles on different LCO surface sites in the experimental samples, the trends are expected to be in good agreement. The experimental half-wave potentials and theoretical limiting potentials for the strained and unstrained Pt catalysts are presented in Fig. 4D with qualitative agreement. The remaining discrepancies likely arise from the strain distribution, which is not expected to be uniform across all sites on the LCO/ $\text{L}_{0.5}\text{CO}$ substrates. Pt NPs that undergo less strain would still contribute to the total activity.

Given the wide variety of tunable battery electrode materials in existence, and the vast number of catalysts and reactions that can be improved with strain, we demonstrate a highly general approach for studying these effects in the design of next-generation catalytic materials. In addition

to fundamental studies, practical applications can also be extended by including large-scale synthesis and strain-tuning methods such as solution-coating of Pt, aqueous solution electrochemical tuning, or chemical extraction/intercalation of Li ions. Other types of battery electrode materials—such as layered MoS_2 , TiO_2 , Bi_2Se_3 , and black phosphorus—can also be used to greatly extend the scope of this strain-tuning method toward acidic electrocatalysis.

REFERENCES AND NOTES

- M. S. Dresselhaus, I. L. Thomas, *Nature* **414**, 332–337 (2001).
- M. G. Walter *et al.*, *Chem. Rev.* **110**, 6446–6473 (2010).
- R. Bashyam, P. Zelenay, *Nature* **443**, 63–66 (2006).
- J. Greeley *et al.*, *Nat. Chem.* **1**, 552–556 (2009).
- Y. Bing, H. Liu, L. Zhang, D. Ghosh, J. Zhang, *Chem. Soc. Rev.* **39**, 2184–2202 (2010).
- S. Mukerjee, S. Srinivasan, M. P. Soriaga, J. McBreen, *J. Electrochem. Soc.* **142**, 1409–1422 (1995).
- J. Suntivich, K. J. May, H. A. Gasteiger, J. B. Goodenough, Y. Shao-Horn, *Science* **334**, 1383–1385 (2011).
- C. Chen *et al.*, *Science* **343**, 1339–1343 (2014).
- X. Huang *et al.*, *Science* **348**, 1230–1234 (2015).
- V. R. Stamenkovic *et al.*, *Nat. Mater.* **6**, 241–247 (2007).
- V. R. Stamenkovic, B. S. Mun, K. J. J. Mayrhofer, P. N. Ross, N. M. Markovic, *J. Am. Chem. Soc.* **128**, 8813–8819 (2006).
- H. Wang *et al.*, *Proc. Natl. Acad. Sci. U.S.A.* **110**, 19701–19706 (2013).
- Z. Lu *et al.*, *Nat. Commun.* **5**, 4345 (2014).
- P. Strasser *et al.*, *Nat. Chem.* **2**, 454–460 (2010).
- H. Li *et al.*, *Nat. Mater.* **15**, 48–53 (2016).
- D. Voiry *et al.*, *Nat. Mater.* **12**, 850–855 (2013).
- M. Mavrikakis, B. Hammer, J. K. Nørskov, *Phys. Rev. Lett.* **81**, 2819–2822 (1998).
- B. Hammer, J. K. Nørskov, *Adv. Catal.* **45**, 71–129 (2000).
- J. Zhang *et al.*, *J. Phys. Chem. B* **109**, 22701–22704 (2005).
- D. Wang *et al.*, *Nat. Mater.* **12**, 81–87 (2013).
- X. Wang *et al.*, *Nat. Commun.* **6**, 7594 (2015).
- L. Zhang *et al.*, *Science* **349**, 412–416 (2015).
- A. Jackson *et al.*, *ChemElectroChem* **1**, 67–71 (2014).

24. S. Koh, P. Strasser, *J. Am. Chem. Soc.* **129**, 12624–12625 (2007).
 25. I. E. L. Stephens et al., *J. Am. Chem. Soc.* **133**, 5485–5491 (2011).
 26. L. Gan, R. Yu, J. Luo, Z. Cheng, J. Zhu, *J. Phys. Chem. Lett.* **3**, 934–938 (2012).
 27. Q. Jia et al., *ACS Nano* **9**, 387–400 (2015).
 28. M. Du, L. Cui, Y. Cao, A. J. Bard, *J. Am. Chem. Soc.* **137**, 7397–7403 (2015).
 29. L. Yang et al., *Sci. Rep.* **4**, 5649 (2014).
 30. C. K. Chan et al., *Nat. Nanotechnol.* **3**, 31–35 (2008).
 31. T. Ohzuku, A. Ueda, *J. Electrochem. Soc.* **141**, 2972–2977 (1994).
 32. G. Csányi, P. B. Littlewood, A. H. Nevidomskyy, C. J. Pickard, B. D. Simons, *Nat. Phys.* **1**, 42–45 (2005).
 33. S. Choi, A. Manthiram, *J. Electrochem. Soc.* **149**, A162–A166 (2002).
 34. Y. Shao-Horn, L. Croguennec, C. Delmas, E. C. Nelson, M. A. O’Keefe, *Nat. Mater.* **2**, 464–467 (2003).
 35. Materials and methods are available as supplementary materials on Science Online.
 36. S. M. George, *Chem. Rev.* **110**, 111–131 (2010).
 37. A. Asthagiri, D. S. Sholl, *J. Chem. Phys.* **116**, 9914–9925 (2002).
 38. S. T. Christensen et al., *Small* **5**, 750–757 (2009).
 39. The nonepitaxial growth does not necessarily mean that the interaction between Pt and LCO/L_{0.5}CO is not strong enough to transfer lattice strain. The Pt atoms on the edge sites of LCO or L_{0.5}CO substrates can form strong bonding with dangling O or Co atoms.
40. K. Zhao, M. Pharr, J. J. Vlassak, Z. Suo, *J. Appl. Phys.* **108**, 073517 (2010).
 41. F. Xiong et al., *Int. J. Electrochem. Sci.* **7**, 9390–9400 (2012).
 42. L. Wang et al., *Nat. Commun.* **4**, 2413 (2013).
 43. V. Viswanathan, H. A. Hansen, J. Rossmeist, J. K. Nørskov, *ACS Catal.* **2**, 1654–1660 (2012).
 44. L. Li, F. Abild-Pedersen, J. Greeley, J. K. Nørskov, *J. Phys. Chem. Lett.* **6**, 3797–3801 (2015).
 45. J. K. Nørskov et al., *J. Phys. Chem. B* **108**, 17886–17892 (2004).
 46. V. Viswanathan, H. Hansen, *Top. Catal.* **57**, 215–221 (2014).

ACKNOWLEDGMENTS

We acknowledge support from the Global Climate Energy Project at Stanford University. H.W. acknowledges support from the Stanford Interdisciplinary Graduate Fellowship. S.X. and F.B.P. were supported by the Center on Nanostructuring for Efficient Energy Conversion (CNEEC) at Stanford University, an Energy Frontier Research Center funded by the U.S. Department of Energy (DOE), Office of Science, Basic Energy Sciences, under award DE-SC0001060. F.A.-P. and J.K.N. acknowledge financial support from the DOE, Office of Basic Energy Sciences, to the SUNCAT Center for Interface Science and Catalysis. C.T.

acknowledges support from the National Science Foundation Graduate Research Fellowship Program (GRFP) grant DGE-114747. Y.C. acknowledges support to initiate the catalysis research from the DOE, Basic Energy Sciences, Materials Sciences and Engineering Division, under contract DE-AC02-76SF00515. The authors acknowledge the help of aberration-corrected STEM-HAADF from P. Yang and Y. Yu at the National Center for Electron Microscopy at the Molecular Foundry. Work at the Molecular Foundry was supported by the DOE Office of Science, Office of Basic Energy Sciences, under contract DE-AC02-05CH11231. The authors also acknowledge helpful discussions with M. Logar. All of the data are available in the main paper and supplementary materials.

SUPPLEMENTARY MATERIALS

www.sciencemag.org/content/354/6315/1031/suppl/DC1
 Materials and Methods
 Figs. S1 to S30
 Table S1
 References (47–58)

13 December 2015; resubmitted 28 March 2016
 Accepted 17 October 2016
 10.1126/science.aaf7680

AUTOPHAGY

The ATG conjugation systems are important for degradation of the inner autophagosomal membrane

Kotaro Tsuboyama,^{1*} Ikuko Koyama-Honda,^{1*} Yuriko Sakamaki,² Masato Koike,³ Hideaki Morishita,¹ Noboru Mizushima^{1†}

In macroautophagy, cytoplasmic contents are sequestered into the double-membrane autophagosome, which fuses with the lysosome to become the autolysosome. It has been thought that the autophagy-related (ATG) conjugation systems are required for autophagosome formation. Here, we found that autophagosomal soluble *N*-ethylmaleimide-sensitive factor attachment protein receptor (SNARE) syntaxin 17-positive autophagosome-like structures could be generated even in the absence of the ATG conjugation systems, although at a reduced rate. These syntaxin 17-positive structures could further fuse with lysosomes, but degradation of the inner autophagosomal membrane was significantly delayed. Accordingly, autophagic activity in ATG conjugation-deficient cells was strongly suppressed. We suggest that the ATG conjugation systems, which are likely required for the closure (i.e., fission) of the autophagosomal edge, are not absolutely essential for autolysosome formation but are important for efficient degradation of the inner autophagosomal membrane.

Macroautophagy (hereafter, autophagy) is a highly inducible intracellular degradation system (1–3). First, a flat membrane sac, termed the isolation membrane or the phagophore, elongates, bends, and sequesters a part of the cytoplasm. Then, its edge is closed by membrane fission to form the double-membrane structure, the autophagosome (4). The autophagosome fuses with lysosomes

and becomes the autolysosome. Lysosomal enzymes selectively degrade the inner autophagosomal membrane (IAM), but not the outer autophagosomal membrane (OAM), and then finally degrade the enclosed cytoplasmic contents.

To characterize autophagosome maturation in mammalian cells, we used the autophagosomal soluble *N*-ethylmaleimide-sensitive factor attachment protein receptor (SNARE) syntaxin 17 (STX17) as an autophagosome marker (5). Elongating isolation membranes were microtubule-associated protein light chain 3 (LC3) positive but STX17 negative (Fig. 1A, red arrows, and movie S1) (5). Later, STX17 was recruited to the whole circumference of ring-shaped structures (Fig. 1A, green arrows). The shape of elongating isolation membranes was elliptical but became almost completely spherical when STX17 was

recruited (Fig. 1B). We hypothesize that fission between the OAM and IAM during the closure of the autophagosomal edge causes a morphological change into stable spherical bodies that occurs immediately before or after the recruitment of STX17.

After STX17 recruitment, several small LAMP1-positive lysosomes (or late endosomes) associated with the autophagosomes (Fig. 1C, 2 to 8 min, blue arrows). Then, the autophagosomal membrane became LAMP1-positive (Fig. 1C, 10 to 16 min, blue arrows). At almost the same time, these structures became positive for LysoTracker Red (LTR), a weak-base probe for acidic compartments. The LTR signals appeared also as ring-shaped structures on the STX17-positive structures (Fig. 1C, 4 to 10 min, red arrows), which suggests that the space between the OAM and IAM is acidified. Next, the ring-shaped LTR signal collapsed, and the lumen of the autolysosomes filled with LTR, which indicated the IAM degradation (Fig. 1C, 12 to 16 min). The STX17 signal gradually disappeared after the collapse of the LTR ring structure (Fig. 1C, 12 to 14 min). This STX17 dissociation was independent of luminal acidification because it was not affected by bafilomycin A₁ treatment (fig. S1). Thus, we detected four steps during autophagosome maturation: STX17 recruitment (step a), lysosomal fusion (step b), IAM degradation (step c), and STX17 release (step d) (Fig. 1C). The total lifetime of STX17 (steps a to d) and the durations (means ± SEM) between each step (a to b, b to c, and c to d) were 11.0 ± 0.6, 2.1 ± 0.3, 6.6 ± 0.6, and 2.2 ± 0.2 min, respectively (Fig. 1C).

Autophagosome formation requires the two ubiquitin-like systems: the ATG12 conjugation system and the ATG8 (LC3s and γ -aminobutyric acid receptor-associated proteins in mammals) conjugation system (6, 7). Ubiquitin-like ATG12 and ATG8 are covalently conjugated to ATG5 and phosphatidylethanolamine (PE), which are catalyzed by the common E1-like protein ATG7 and the specific E2-like proteins ATG10 and ATG3, respectively. Conjugation of ATG8 or LC3 with

¹Department of Biochemistry and Molecular Biology, Graduate School and Faculty of Medicine, The University of Tokyo, Tokyo 113-0033, Japan. ²Research Center for Medical and Dental Sciences, Tokyo Medical and Dental University, Tokyo 113-8510, Japan. ³Departments of Cell Biology and Neuroscience, Juntendo University Graduate School of Medicine, Bunkyo-Ku, Tokyo 113-8421, Japan.

*These authors contributed equally to this work.

†Corresponding author. Email: nmizu@m.u-tokyo.ac.jp

EXTENDED PDF FORMAT
SPONSORED BY



Direct and continuous strain control of catalysts with tunable battery electrode materials

Haotian Wang, Shicheng Xu, Charlie Tsai, Yuzhang Li, Chong Liu, Jie Zhao, Yayuan Liu, Hongyuan Yuan, Frank Abild-Pedersen, Fritz B. Prinz, Jens K. Nørskov and Yi Cui (November 24, 2016)
Science **354** (6315), 1031-1036. [doi: 10.1126/science.aaf7680]

Editor's Summary

Tuning nanoparticle strain

The catalytic activity of metals in heterogeneous catalysts can be altered by applying strain, which changes the crystalline lattice spacing and modifies the metal's electronic properties. Wang *et al.* show how particles of cobalt oxide, a positive electrode for lithium batteries, can expand or contract with charging and transfer strain to adsorbed platinum nanoparticles. For the oxygen reduction reaction used in fuel cells, compressive strain boosted activity by 90%, and tensile strain decreased it by 40%.

Science, this issue p. 1031

This copy is for your personal, non-commercial use only.

- Article Tools** Visit the online version of this article to access the personalization and article tools:
<http://science.sciencemag.org/content/354/6315/1031>
- Permissions** Obtain information about reproducing this article:
<http://www.sciencemag.org/about/permissions.dtl>

Science (print ISSN 0036-8075; online ISSN 1095-9203) is published weekly, except the last week in December, by the American Association for the Advancement of Science, 1200 New York Avenue NW, Washington, DC 20005. Copyright 2016 by the American Association for the Advancement of Science; all rights reserved. The title *Science* is a registered trademark of AAAS.